

# LOGen: Toward LiDAR Object Generation by Point Diffusion

Ellington Kirby<sup>1</sup>, Mickael Chen<sup>1</sup>, Renaud Marlet<sup>1,2</sup>, Nermin Samet<sup>1</sup>

<sup>1</sup>Valeo.ai, Paris, France <sup>2</sup>LIGM, Ecole des Ponts, Univ Gustave Eiffel, CNRS, Marne-la-Vallée, France

<https://nerminsamet.github.io/logen/>

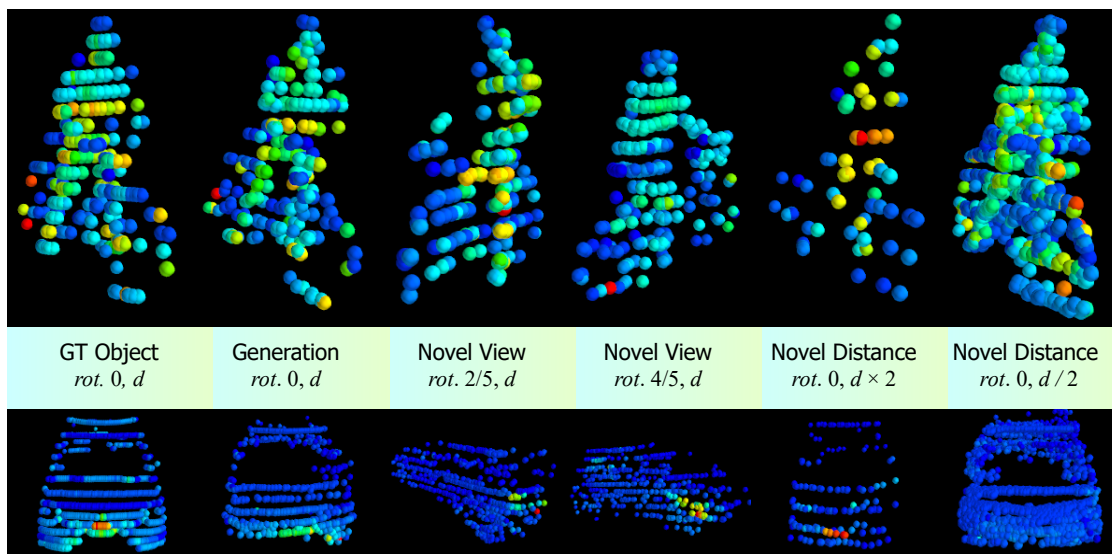


Figure 1. **Novel LiDAR objects generated by LOGen** using the conditioning information of real objects from the nuScenes validation set. Top row shows a bicycle (car on bottom row) generated via interpolations of conditioning information. Relative to the sensor,  $rot$  is the object’s rotation while  $d$  is the distance. Color is according to LiDAR intensity. More examples in Appendix.

## Abstract

The generation of LiDAR scans is a growing area of research with diverse applications to autonomous driving. However, scan generation remains challenging, especially when compared to the rapid advancement of 2D and 3D object generation. We introduce a novel task: LiDAR object generation, requiring models to produce 3D objects as viewed by a LiDAR scan. This task focuses LiDAR scan generation on the most interesting aspect of scenes, the objects, while also benefiting from advancements in 3D object generative methods. We introduce a novel diffusion-based model to produce LiDAR point clouds of dataset objects, including intensity, and with an extensive control of the generation via conditioning information. Our experiments on nuScenes show the quality of our generations measured with new 3D met-

rics developed to suit LiDAR objects.

## 1. Introduction

As 2D generative methods have exploded in their capacity to generate diverse and high quality images [32], one area of focus for 3D object generation has been understudied: objects in the context of LiDAR sensors. LiDAR is an essential modality for autonomous agents in driving scenarios. It provides accurate 3D information about the environment while being robust to adverse light conditions, making it crucial for safe navigation. The utility and corresponding shortcomings of LiDAR datasets [21, 28] makes the generation of LiDAR objects interesting from a variety of perspectives (sensor level generation for simulation [26], rare class augmentation [54], out-of-distribution generation [22], corner case generation [19], object disentanglement [30] etc.).

Objects perceived by LiDAR sensors are distinct from classically rendered 3D objects in the impact that the relative angle and distance of objects to the sensor has on the final appearance of an object [57]. While generated 3D meshes are uniform volumes, LiDAR objects have unique appearances depending on the intersection of the beam and the visible face of the object. Further, LiDAR objects contain an additional fourth channel of information when compared to classic 3D objects: the intensity of the laser beam reflected back to the sensor. Models which generate LiDAR objects must be capable of using this relative positioning and creating the intensity channel in order to generate realistic objects [46].

LiDAR object generation thus explores the latent capability of generative models to understand complex 3D relationships between objects, as capturing the resulting appearance of an object via a LiDAR sensor requires understanding the interplay of angle, distance, and orientation between the sensor and the object. Generating objects utilizing this geometric view conditioning is a more challenging evaluation of 3D generative methods [42].

The generation of LiDAR data has been explored most extensively at the scene level, where many works have attempted to generate entire novel scans of autonomous vehicles in new surroundings [51, 57, 58]. However LiDAR scene generation remains a difficult task, with many works turning towards simplifying assumptions to focus the generative task onto more tractable footing [29, 31, 34, 47, 53]. We propose to bring recent advancements in generative methods [5, 27] to the domain of LiDAR data, focusing on the generation of high quality and realistic LiDAR objects.

We introduce a transformer-based diffusion model, dubbed LOGen (for LiDAR Object Generator), which is designed to generate LiDAR scans of new objects. The generation is parameterized by the object class, angle, and distance from which objects are seen by the LiDAR sensor. This conditioning allows fine grained control of the appearance of the generated objects.

To the best of our knowledge there is no previous work on this topic. As we are the first to tackle this task, we compare LOGen against suitable alternatives that we design, inspired from other tasks: a sparse 3D CNN (MinkUNet [6]); a 2D transformer-based generator (PixArt- $\alpha$  [5]) adapted to 3D; and a 3D transformer-based generator (DiT-3D [27]), originally designed for traditional 3D objects, which we adapt to LiDAR objects. We show the quality of our generated objects compared to these baselines. We also evaluate at scene level on the semantic segmentation task to assess the realism of objects we generate.

Our contributions are as follows:

- We are the first to propose a diffusion-based method specifically designed to produce LiDAR point clouds of objects, including intensity and with an extensive control of the generation (conditioning).
- We propose a new transformer-based LiDAR object diffusion model, operating on 3D points, as well as three other diffusion-based baselines.
- Our experiments on nuScenes [3] show that despite the compact size of our model (just 7.5m parameters), we achieve superior quality, which we also measure with new metrics more suited to LiDAR objects.

We believe that the LiDAR object generation task is ripe for future exploration, and the promising results we present here will serve as a basis for this task.

## 2. Related Work

**3D object generation.** Various techniques have been proposed for 3D object generation: GANs [1, 37], VAEs [20, 44], normalizing flows [52], diffusion at point level [25, 42], and diffusion on features at voxel level with a transformer architecture [27]. However, these methods are only typically evaluated on datasets such as ShapeNet [4], ModelNet [48], or CO3D [35] after sampling points uniformly on shape surfaces, rather than following LiDAR sampling patterns. Their behavior with uneven point distributions of (sensor-specific) LiDAR scans is unexplored.

These methods do not use geometric conditioning related to viewpoint and do not generate point intensities. Further, most of these methods are trained and evaluated with a high and fixed number of points: typically 2048. It is not clear how they would behave with varying and sparse point clouds, as is the case of LiDAR objects. Only PointFlow intrinsically supports the generation of an arbitrary number of points, but it is also trained and evaluated on 2048 points [52].

**LiDAR scan generation.** Methods have been proposed to generate full LiDAR scans, by LiDAR simulation [11] in synthetic environments [53], or by learning to generate LiDAR data using energy-based models [57], VQ-VAEs [51], diffusion in range images [15, 29, 34] or diffusion on 3D points [31], possibly with images [55]. Further, simulation and learning can be combined to improve realism [26, 58]. As our work focuses on objects from existing datasets, scene-level generation serves as a source of inspiration but is not a direct comparison.

Some scan generation methods can be conditioned on a semantic map [34], or can place learned codes of

object classes into a canvas representing the scene before decoding [51]. But this instance-level conditioning offers little control on object generation and it does not provide a way to augment an existing point cloud. [47] introduces text based conditioning in LiDAR scan generation, but does not evaluate the fidelity of the conditional generations, providing only qualitative evaluations of generated objects in scenes.

**LiDAR object simulation.** LiDAR simulation on manmade CAD objects has been proposed to add variation to objects inserted into scenes [8, 9]. However these approaches are rigid in that CAD shapes have to match the object shape distribution in the region of the world where the original scans were captured. Moreover, this approach does not handle intensity: it only produces 3D point coordinates, not intensities. LiDARSim [26] tackles the problem of LiDAR simulation from a data driven approach similar to LOGen, however still more broadly at the scene level. They take a physics based approach to simulate LiDAR, then learn the resulting raydrop to produce realistic scans including intensity. Our approach directly learns object appearance and intensity from the data at an object level, eliminating the need for physics based simulation and collecting 3D objects.

**LiDAR object generation.** To the best of our knowledge, only [49] considers the specific question of LiDAR object generation. The paper actually proposes five methods, based on a Gaussian mixture model (GMM), a variational auto-encoder (VAE), a latent generative adversarial network (L-GAN), an adversarial auto-encoder (AAE), and point cloud diffusion based on U-Net (PCD) for which no code is available. All these methods have significant limitations. First, they offer no conditioning, and generated points have no dimension nor intensities. Training objects must have 2048 points: objects with more points are downsampled, objects with less points get duplicated points, and objects with less than 256 points are ignored, while we go down to as few as 20 points. Evaluation is only at object level, with a classification task, not at scene level, and only 5 categories are evaluated, some with merged classes to ensure “sufficient granularity” (e.g., motorcycles with bicycles), while we do it on all 10 object classes of nuScenes.

### 3. Method

The goal of the *LiDAR object generation task* is to learn, for known classes in a labeled LiDAR dataset, to generate 3D point clouds of novel objects, as they would be captured by the same LiDAR sensor from arbitrary

viewpoints. The training distribution is given by real-world objects extracted from 3D scans.

We train a diffusion model to generate point clouds of novel objects. The diffusion process is applied directly on points given as input, and is conditioned by geometric information concerning the object to generate.

#### 3.1. Object parameterization

An object in a LiDAR dataset is given by its class  $c$ , a set of 3D points with intensities, as well as information on the object bounding box, namely, the box center  $(x, y, z)$ , the box length, width and height  $(l, w, h)$  and the box yaw  $\psi$ , i.e., the orientation around the vertical  $z$  axis (azimuth) of the heading of the object.

**Parameters.** To reduce the number and variability of input and conditioning parameters when training a model, we normalize the representation of objects with respect to the sensor location. For this, the Cartesian coordinates of object points are made relative to the oriented box center, i.e., relative to the box center and rotated around the  $z$  axis to align with the object box heading. The intensities are scaled according to the log-max.

We also decrease the number of parameters regarding the box center location and orientation as the object appearance, seen from the sensor, only depends on the distance  $d$  to the object and on the observation angle  $\phi$ , i.e., the angle between the object heading  $\psi$  and the ray from the object bounding box center to the sensor. (As an illustration,  $\phi = 0$  means the object is facing the sensor, regardless of the object location around the ego vehicle.) In this conversion from Cartesian to cylindrical coordinates, the altitude  $z$  of the box center is kept.

In the end, the data distribution to learn consists of objects represented by a set of points  $s = \{P_i\}_{i=1}^N$  in  $\mathbb{R}^{N \times 4}$  with (centered) Cartesian coordinates and intensities. Moreover, we condition the generation on the following box information:  $\kappa = (\phi, d, z, l, w, h)$ . Class  $c$  is not directly included as we train one model per class.

We do not normalize the point coordinates inside the object box, e.g., in  $[0, 1]$ . This preserves the absolute dimensions of objects and the specificity of the LiDAR scanning patterns, depending in particular on the distance to the sensor. Consequently, the diffusion model is not constrained to generate points only inside the box. Experiments however show that only a few generated points sometimes fall out of the box, but not very far.

**Point embedding.** The way to embed points for diffusion has strong implications on the memory consumption and realism of generated outputs.

DiT-3D [27] introduces voxel embeddings that efficiently structure and aggregate points into patches.

This technique, alongside window attention, allows the model to compute attention across shapes of thousands of points. The de-voxelization procedure places points in a final position inside their voxel, based on a weighted average of their activations. It has the effect of creating uniform and smooth point clouds across the underlying surface. Such uniform distributions are ideal for the goal of producing a continuous 3D mesh, but do not match the banded pattern observed when a LiDAR captures objects in the real world.

To address this issue, we introduce a simple embeddings based on PointNet [33]. These features are just the output of a single 1D convolution, with which we project from our input dimension (3+1) into the embedding dimension. Because the point clouds (averaging from 40 points for bikes to 463 for bus) are in general magnitudes smaller than the point clouds generated in the original DiT-3D paper (thousands of points), we can use standard memory-efficient attention layers and avoid the need for voxelization. In the experiment section, we examine the impact of both types of embeddings.

**Conditioning encoding.** A key stage when using diffusion is the encoding of the conditioning and time step. Classically, we rely on Fourier features [40], which involves a higher dimensional projection followed by a sine/cosine encoding of the corresponding features. This applies to all scalar values of the condition but angle  $\phi$ . To account for the periodic discontinuity of representation for an angle, we encode  $\phi$  using the cyclical embeddings from [18], which preserves the cyclical nature of angular data. In our experiments, we train one network per class; we thus do not need to encode the class.

### 3.2. LiDAR object diffusion

Given a dataset with a number of object point clouds  $S = \{s_j\}_{j=1}^M$  alongside conditions  $K = \{\kappa_j\}_{j=1}^M$ , the objective is to learn the conditional distribution  $p(S|K)$ . This is done via a Denoising Diffusion process: we learn to denoise input 4D Gaussian noise ( $N$  noisy points) into a target shape ( $N$  points representing a scanned object).

We rely on the time-discrete formulation of the diffusion process known as Denoising Diffusion Probabilistic Models (DDPM) [14], which is also used in DiT-3D [27] and in LiDAR scene generation methods [31]. We only sketch this formulation below. More details can be found in [14, 25] and in Appendix.

During training, we sample a random time step  $t$  and produce, via a forward noising process, a noisy sample  $s_t$  of an input object point cloud  $s_0 = s$ . This forward noising process is a known Gaussian process  $q(s_t|s_{t-1})$  for which it is possible to directly create

noisy samples  $s_t = \sqrt{\bar{\alpha}_t}s_0 + \sqrt{1 - \bar{\alpha}_t}\epsilon_0$  where  $\epsilon_0 \sim \mathcal{N}(\mathbf{0}, \mathbf{I})$  is Gaussian noise,  $\bar{\alpha}_t = \prod_{i=1}^t (1 - \beta_i)$ , and  $0 < \dots < \beta_t < \dots < \beta_T < 1$  is a noise scaling schedule.

The reverse process is provided by a denoising network with parameters  $\theta$ . The goal is to learn a distribution of the form  $p_\theta(s_{t-1}|s_t) = \mathcal{N}(s_{t-1}|\mu_\theta(s_t, t), \sigma_t^2 \mathbf{I})$ . This is learned via optimizing the evidence variational lower bound, that simplifies to minimizing the Kullback-Leibler divergence between the forward and reverse processes. After simplification, it boils down to minimizing a mean-squared loss between the model output  $\hat{\epsilon}_\theta(s_t, t)$  and the ground-truth Gaussian noise  $\epsilon_0$ . Given  $\hat{\epsilon}_\theta(s_t, t)$ , we can then compute  $\mu_\theta(s_t, t)$  and get a denoising step recurrence equation defining  $s_{t-1}$  from  $s_t$  (cf. Appendix).

A training step consists of sampling a different random time step  $t$  for each element of the batch, producing the noised samples, and using the denoising neural network to predict the output of the reverse process.

To exploit conditioning, the above formulation is extended with the extra input of a condition  $\kappa$ , leading to a denoising network  $\hat{\epsilon}_\theta(s_t, t, \kappa)$ . To apply the conditional guidance, we follow the Classifier Free Guidance formulation from [13]. This implies the dropout of conditioning information during the training procedure, where all conditions are replaced by a pre-defined null embedding. Using the null embedding results in an unconditioned pass of the model. A parameter  $\lambda$  controls the strength of the guidance. The final predicted noise for a time step  $t$  is computed as:  $\epsilon_\theta(s_t, t, \kappa) = \lambda \hat{\epsilon}_\theta(s_t, t, \kappa) + (1 - \lambda) \hat{\epsilon}_\theta(s_t, t, \emptyset)$ .

### 3.3. Architecture

DiT-3D [27] is straightforwardly derived from DiT [32], and thus shares a similar architecture. PixArt- $\alpha$  [5] adds cross attention to DiT to inject conditions. Our baselines DiT-3DL and PixArt-L are directly adapted from their original counterparts to handle: (i) LiDAR data, i.e., point embedding, and (ii) LiDAR object conditioning. LOGen is then a modification of PixArt-L, as described below. The conditioning  $\kappa = (\phi, d, z, l, w, h)$  is applied in the denoising network to direct the generative process. Given the importance of the conditioning in our task, we explore three variants in the architecture design space.

- *AdaLN-Zero* is the best-performing guidance method proposed in DiT [32], and reused in DiT-3D. In our case, for DiT-3DL, the six conditioning values are concatenated to the time step and used to learn the adaptive layer-norm shift and scale parameters.
- *AdaLN-single* is the guidance proposed and used in PixArt- $\alpha$  [5]. This guidance relies on the addition of



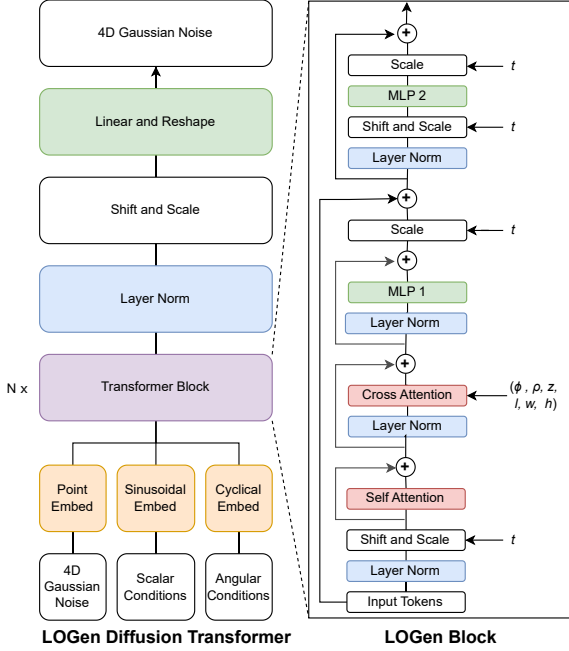


Figure 2. Architecture of LOGen. For architectures of our baselines PixArt-L and DiT-3DL please refer to Appendix.

cross-attention layers which attend between the embedded noisy points and the conditioning information. While in the adaptive layer norm the conditions are always used to learn global shift and scale parameters, cross-attention layers allow the model to learn the guidance on a local scale. We do the same in PixArt-L.

- We observe that the separation of the self-attention layers from the cross-attention layers by a scale operation in the PixArt-L architecture degrades the generation results (cf. Tab. 1 and 2). Thus we introduce a third type of conditioning in LOGen blocks, where we apply the cross attention immediately after the self-attention layer, and scale after these operations. The full *LOGen architecture* is shown in Fig. 2.

## 4. Experiments

### 4.1. Experimental Setup

**Dataset.** We evaluate our approach on nuScenes [3], which was acquired with a 32-beam LiDAR, thus creating notably sparse sweep patterns. To construct object samples, we use the semantic point labels and the 3D box annotations of objects. We take as object instance all points falling into a box, filtering out possible points of a different class. We also discard objects with less than 20 points. Point intensity, which ranges in 0–255, has a highly irregular distribution, with most examples

clustered from 0–30, and with outliers. To create a more uniform intensity distribution, we use log max scaling.

In total, we extract 268,684 objects with at least 20 points which covers more than 95% of all object points. It can also be noted that the official instance segmentation evaluation of nuScenes only considers instances with at least 15 points [3]. In order to unify the number of points per cloud in a batch, we pad each point cloud to the max length in the batch. For all experiments we use the conditioning information from objects in the validation set, approximating novel views of objects.

**Object-level metrics.** To evaluate the ability to generate a sensible variant of a real object given only the conditioning information corresponding to the real object, we use two pointset metrics: Chamfer Distance (**CD**) and Earth Mover’s Distance (**EMD**). These metrics penalize incoherent shape generations which diverge from original objects, however also penalizing realistic but diverse generations. To then evaluate the realism of generations, we use different distribution-based metrics which compare the set of real objects of a given class to a corresponding set of objects generated with the associated conditioning.

We use the Fréchet PointNet Distance (**FPD**) [37], an adaptation of the classic Fréchet Inception Distance (FID) [12] by replacing 2D Inception features with 3D PointNet features [33]. However, the original FPD used as reference relies on the original PointNet classifier, trained on ModelNet40 [33]. While it is well suited for use on objects generated from a 3D shape dataset, with dense and uniform point sampling, it is not for LiDAR-scanned objects. We thus use instead a separate PointNet classifier trained on the real LiDAR objects of nuScenes.

We also measure the Accuracy of that same PointNet Classifier (**APC**), i.e., trained on real objects, for recognizing synthetic objects. It is to be compared to the accuracy of the classifier for recognizing real objects.

We additionally consider the Kernel Inception Distance (KID), which has advantages over FID, in particular for small datasets [2]. Like for FID, we adapt KID into a Kernel PointNet Distance (**KPD**), replacing the Inception network by our trained PointNet.

Besides the above metrics, which compare the distributions of real and synthetic objects at feature level, we also consider distribution comparisons at a pointset level. We use coverage (**COV**) [1], which measures the proportion of real pointsets matched to at least one generated pointset, and 1-nearest neighbor accuracy (**1-NNA**) [52], derived from [23], which merges real and synthetic objects and counts the proportion of closest neighbors of each sample that are of the same source.



Figure 3. Comparisons of real objects and generated output for all ten classes. Note that the LOGen is able to both capture the LiDAR pattern and generate objects of varying scales and shapes. Other models produce outputs with a degraded LiDAR pattern or do not generate coherent examples of rare classes such as bikes, motorcycles and trucks.

Model	Emb.	CD ↓ EMD ↓		1-NNA(%) ↓		COV(%) ↑		Intensities	
		CD	EMD	CD	EMD	CD	EMD	1-NNA ↓	COV ↑
MinkUNet	-	0.208	0.212	79.5	74.4	33.7	41.7	N/A	N/A
PixArt-L	PE <sub>4ch</sub>	0.196	0.204	76.5	72.5	33.5	41.8	71.6	32.9
DiT-3DL	VE <sub>3ch</sub>	0.136	0.121	75.8	70.9	34.3	42.0	N/A	N/A
DiT-3DL	PE <sub>4ch</sub>	0.142	0.125	<b>73.4</b>	70.7	35.5	42.1	74.4	31.4
LOGen	PE <sub>4ch</sub>	<b>0.130</b>	<b>0.111</b>	74.1	<b>70.6</b>	<b>36.0</b>	<b>42.3</b>	<b>68.2</b>	<b>37.0</b>

Table 1. **Point-based metrics.** Mean classwise score for CD, EMD, 1-NNA, COV. Emb.: type of point embedding: none (-), voxel-based (VE<sub>3ch</sub>) or PointNet-based (PE<sub>4ch</sub>). The last two columns report 1-NNA and COV scores for intensity histograms based on CD.

Model	Emb.	FPD ↓		KPD (%) ↓		APC (%) ↑	
		3 ch.	4 ch.	3 ch.	4 ch.	3 ch.	4 ch.
MinkUNet	-	25.4	N/A	3.18	N/A	22.6	N/A
DiT-3DL	VE <sub>3ch</sub>	2.80	N/A	0.25	N/A	39.8	N/A
DiT-3DL	PE <sub>4ch</sub>	2.62	6.99	0.25	0.75	37.2	41.7
PixArt-L	PE <sub>4ch</sub>	2.95	5.16	0.24	0.41	37.8	45.5
LOGen	PE <sub>4ch</sub>	<b>1.34</b>	<b>2.18</b>	<b>0.10</b>	<b>0.12</b>	<b>40.9</b>	<b>48.1</b>
Real dataset objects		-	-	-	-	39.0	46.4

Table 2. **Feature-based metrics.** Mean classwise scores for FPD, KPD, APC. Emb.: type of point embedding: none (-), voxel-based (VE<sub>3ch</sub>) or PointNet-based (PE<sub>4ch</sub>).

1-NNA ranges from 100% when distributions are separate, to 50% when they are indistinguishable. It evaluates both diversity and quality in a single metric. COV and 1-NNA are measured with CD and EMD.

We extend COV and 1-NNA to measure the quality of the generated intensities. We extract 256-dimensional normalized intensity histograms from generated objects to use as features for COV and 1-NNA computations. The Appendix details all metrics.

**Scene-level metrics.** A second set of evaluations is conducted on the perception of generated objects in a scene context by a typical 3D segmentation model with the contention that more realistic objects should be segmented at a similar rate to real objects. We consider the replacement of ground-truth objects by objects generated with the same conditioning, then measure the change in classwise **mIoU** segmentation performance of the model on this modified data. We use a variant of nuScenes, nuScenes (LOGen), where each object with at least 20 points is replaced by a generated object of the same class and box size, seen under the same viewing angle, and with the same number of points.

As segmenter, we use the popular SPVCNN [41], which has been widely used in evaluation settings [36, 43, 50]. We consider two different versions: **SPVCNN<sub>3ch</sub>** trained on points coordinates only, while **SPVCNN<sub>4ch</sub>** is also trained using point intensities.

Distance to sensor	FPD ↓		KPD (%) ↓		APC (%) ↑	
	3 ch.	4 ch.	3 ch.	4 ch.	3 ch.	4 ch.
orig. ( $d$ )	1.34	2.18	0.10	0.12	40.9	48.1
$d \times 2$	4.79	12.70	0.61	1.71	34.0	38.4
$d / 2$	3.08	8.13	0.33	0.85	38.3	49.8

Table 3. **Evaluation of conditioning on distance to sensor.** LOGen generates realistic instances at varying distances. Note that the distribution of objects has diverged from the GT as objects are more or less dense according to the point size scaling, especially in the  $d \times 2$  case, where the point clouds have become much sparser.

**Baselines.** Given the novelty of the task, we construct the following baselines: **MinkUNet** is the sparse convolutional architecture used in LiDiff [31], which ignores intensities. **PixArt-L** is our adaptation of PixArt- $\alpha$  to LiDAR points and conditioning, using our PointNet embeddings (PE) to allow generation of intensities. **DiT-3DL VE<sub>3ch</sub>** is our adaptation of DiT-3D to LiDAR conditioning, i.e., with its original voxel embeddings (VE) and no handling of intensities. (The voxelization library used in DiT-3D [27] does not handle a fourth input channel; handling intensities would require adapting the voxelization layer like in MinkUNet [6], as separate input features.) **DiT-3DL PE<sub>4ch</sub>** replaces VE by our PE in DiT-3DL VE<sub>3ch</sub>, and thus also handles intensities.

## 4.2. Object-level evaluation

Qualitative generation examples are shown in Fig. 3 and Fig. 4.

**Point embeddings.** Tab. 1 and 2 show that the voxel embeddings of DiT-3D do not perform as well as our PointNet embeddings, which supports our proposal (Sec. 3.3). MinkUNet succeeds in generating local structure (LiDAR pattern), but fails to generate objects respecting size conditions. The lack of point embeddings in MinkUNet create global size inconsistencies.

**Architecture.** Tab. 1 shows that LOGen transformer blocks perform slightly better than the blocks proposed in PixArt- $\alpha$  and DiT-3D. Tab. 2 shows that the superiority of LOGen blocks is more pronounced as measured by the feature-based metrics of FPD and KPD.

**Evaluation of conditioning on distance to sensor.** To assess the quality of generated objects at varying sensor distances, we created two variants at distances  $2 \times d$  and  $d / 2$  where  $d$  is the original object distance. We scale the number of points from the initial size according to a power law [7] as the distance changes. Since ground truths at these distances are unavailable, we evaluate

	Model	Emb.	bar.	bic.	bus	car	c.veh	mot.	ped.	t.con.	tra.	tru.	mean
3 channel	MinkUNet		76.1	31.4	18.7	<b>84.4</b>	14.7	63.6	69.8	59.3	12.4	49.7	48.0
	DiT-3DL	VE <sub>3ch</sub>	48.4	42.5	0.3	34.1	0.2	63.8	75.6	69.6	7.7	3.4	34.6
	DiT-3DL	PE <sub>4ch</sub>	61.6	39.2	11.1	84.2	1.7	68.8	77.5	51.3	15.9	26.6	43.9
	PixArt-L	PE <sub>4ch</sub>	58.9	32.1	3.9	75.7	0.9	76.6	79.0	56.7	13.6	51.3	44.9
	LOGen	PE <sub>4ch</sub>	<b>78.2</b>	<b>50.9</b>	<b>60.1</b>	79.1	<b>28.1</b>	<b>82.2</b>	<b>84.2</b>	<b>73.5</b>	<b>37.5</b>	<b>63.2</b>	<b>63.7</b>
	GT		80.3	48.8	90.7	94.2	40.6	86.0	85.5	73.4	60.7	85.2	74.5
4 channel	DiT-3DL	PE <sub>4ch</sub>	62.5	29.0	18.3	85.9	6.3	62.6	68.4	47.2	15.9	37.7	43.4
	PixArt-L	PE <sub>4ch</sub>	56.6	33.7	14.5	82.4	8.1	78.5	79.3	62.8	26.7	52.6	49.5
	LOGen	PE <sub>4ch</sub>	<b>78.0</b>	<b>48.9</b>	<b>71.7</b>	<b>91.3</b>	<b>37.1</b>	<b>82.0</b>	<b>84.8</b>	<b>79.1</b>	<b>45.1</b>	<b>72.9</b>	<b>69.1</b>
	GT		81.6	50.4	90.9	94.6	44.5	88.1	85.6	77.4	64.6	85.6	76.3

Table 4. **Scene-level comparison.** SPVCNN is trained with 3 or 4 channels (coordinates + intensity) on nuScenes (train set) with real objects. It is tested on nuScenes (val set) where each object ( $\geq 20$  points) is replaced with a generated object of the same class, box size and sensor viewing angle, and with the same number of points, and where objects with less than 20 points are *removed* from the dataset. Also note that, **intensities generated by LOGen** are realistic enough to provide **+5.4 mIoU%** at scene level.

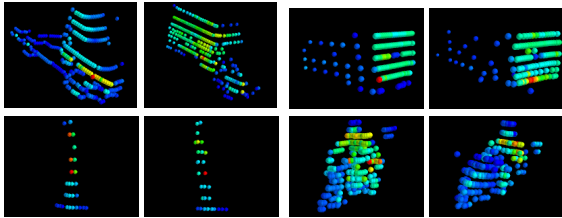


Figure 4. **Examples of generated intensities.** Clockwise: Truck, Bus, Motorcycle, Traffic Cone. For each pair, the left image is from the nuScenes validation set, the right image is generated using the same conditioning information and number of points. More examples can be seen in Appendix.

quality on feature-based metrics (Table 3). Additionally, integrating these objects into scenes for scene-level evaluation is nontrivial due to the distance variation.

For all dataset statistics, class-wise results, and a comparison of single-model-per-class vs. multi-class approaches, please refer to the Appendix.

### 4.3. Scene-level evaluation

**Semantic quality of generated data.** Tab. 4 shows that the LOGen generations are more semantically identifiable from the point of view of an SPVCNN segmenter. Though trained on real objects, the segmenter is able to recognize LOGen objects at a much higher mIoU than other models, +19.6 points versus the second best model. This is particularly pronounced for rare classes such as bicycle, bus, trailer, and construction vehicle.

**Evaluation of conditioning on sensor viewing angle.** To assess LOGen’s ability to generate realistic objects regardless of viewing angle, we modify the synthetic replacements by rotating their angular condition. This re-

Test objects	Box orientation	mIoU (%) $\uparrow$	
		3 ch.	4 ch.
real	orig.	74.5	76.3
LOGen	orig.	63.7	69.1
LOGen	rot. $1/5$	53.7	64.6
LOGen	rot. $2/5$	54.8	66.0
LOGen	rot. $3/5$	53.8	63.8
LOGen	rot. $4/5$	53.3	64.1

Table 5. **Evaluation of conditioning on sensor viewing angle.** SPVCNN is trained with 3 or 4 channels (coordinates + intensity) on nuScenes with real objects. It is tested on nuScenes where each object ( $\geq 20$  points) is replaced with a LOGen-generated object of the same class, box size, and sensor viewing angle, but rotated on itself.

duces the need to find suitable locations for new objects. We consider five evenly spaced angles around a full turn, i.e.,  $i/5 \times 360^\circ$  where  $i \in 0..4$ , as shown in Fig. 1.

Tab. 5 shows a moderate variation of the performance when rotating the objects. This performance is partly due to collisions between objects that occur after rotation (the transformation is performed without such a test). Further, the distribution of object viewing angles in the dataset is not uniform. Less viewed angles can result in noisier generations.

**Limitations.** Currently we train from occluded objects with partly empty bounding boxes without any modifications. Consequently, all objects we generate tend to fill the conditioned bounding box, and thus fill in areas of objects that should be occluded.



## 5. Conclusion

This work demonstrates that a well-designed diffusion model is capable of generating realistic LiDAR objects. Novel metrics, baselines and LOGen (best performing architecture) establish the first standard in LiDAR object generation. Future work can increase generation speed and memory efficiency of the models, and develop novel methods to use generated objects.

## References

- [1] Panos Achlioptas, Olga Diamanti, Ioannis Mitliagkas, and Leonidas Guibas. Learning representations and generative models for 3D point clouds. In *ICML*, 2018. 2, 5, 15
- [2] Mikolaj Binkowski, Danica J. Sutherland, Michael Arbel, and Arthur Gretton. Demystifying MMD GANs. In *ICLR*, 2018. 5, 16
- [3] Holger Caesar, Varun Bankiti, Alex H Lang, Sourabh Vora, Venice Erin Liong, Qiang Xu, Anush Krishnan, Yu Pan, Giancarlo Baldan, and Oscar Beijbom. nuScenes: A multimodal dataset for autonomous driving. In *CVPR*, pages 11621–11631, 2020. 2, 5, 16
- [4] Angel X. Chang, Thomas Funkhouser, Leonidas Guibas, Pat Hanrahan, Qixing Huang, Zimo Li, Silvio Savarese, Manolis Savva, Shuran Song, Hao Su, Jianxiong Xiao, Li Yi, and Fisher Yu. ShapeNet: An information-rich 3D model repository. Technical Report arXiv:1512.03012, Stanford University & Princeton University & Toyota Technological Institute at Chicago, 2015. 2
- [5] Junsong Chen, Jincheng Yu, Chongjian Ge, Lewei Yao, Enze Xie, Yue Wu, Zhongdao Wang, James Kwok, Ping Luo, Huchuan Lu, et al. Pixart- $\alpha$ : Fast training of diffusion transformer for photorealistic text-to-image synthesis. In *ICLR*, 2024. 2, 4, 13, 14
- [6] Christopher Choy, JunYoung Gwak, and Silvio Savarese. 4D spatio-temporal ConvNets: Minkowski convolutional neural networks. In *CVPR*, 2019. 2, 7, 14
- [7] Aaron Clauset, Cosma Rohilla Shalizi, and Mark EJ Newman. Power-law distributions in empirical data. *SIAM review*, 51(4):661–703, 2009. 7
- [8] Jin Fang, Dingfu Zhou, Feilong Yan, Tongtong Zhao, Feihu Zhang, Yu Ma, Liang Wang, and Ruigang Yang. Augmented lidar simulator for autonomous driving. *IEEE Robotics and Automation Letters*, 5(2):1931–1938, 2020. 3
- [9] Jin Fang, Xinxin Zuo, Dingfu Zhou, Shengze Jin, Sen Wang, and Liangjun Zhang. LiDAR-Aug: A general rendering-based augmentation framework for 3D object detection. In *CVPR*, 2021. 3
- [10] Whye Kit Fong, Rohit Mohan, Juana Valeria Hurtado, Lubing Zhou, Holger Caesar, Oscar Beijbom, and Abhinav Valada. Panoptic nusenes: A large-scale benchmark for lidar panoptic segmentation and tracking. *IEEE Robotics and Automation Letters*, pages 3795–3802, 2022. 17
- [11] Michael Gschwandtner, Roland Kwitt, Andreas Uhl, and Wolfgang Pree. BlenSor: Blender sensor simulation toolbox. In *Advances in Visual Computing (ISVC)*, 2011. 2
- [12] Martin Heusel, Hubert Ramsauer, Thomas Unterthiner, Bernhard Nessler, and Sepp Hochreiter. GANs trained by a two time-scale update rule converge to a local Nash equilibrium. In *NeurIPS*, 2017. 5, 16
- [13] Jonathan Ho and Tim Salimans. Classifier-free diffusion guidance. *arXiv preprint arXiv:2207.12598*, 2022. 4, 12, 13
- [14] Jonathan Ho, Ajay Jain, and Pieter Abbeel. Denoising diffusion probabilistic models. In *NeurIPS*, 2020. 4, 12
- [15] Qianjiang Hu, Zhimin Zhang, and Wei Hu. RangeLDM: Fast realistic lidar point cloud generation. In *ECCV*, 2024. 2
- [16] Tero Karras, Samuli Laine, and Timo Aila. A style-based generator architecture for generative adversarial networks. In *Proceedings of the IEEE/CVF conference on computer vision and pattern recognition*, pages 4401–4410, 2019. 13
- [17] Tero Karras, Miika Aittala, Timo Aila, and Samuli Laine. Elucidating the design space of diffusion-based generative models. In *NeurIPS*, 2022. 12
- [18] Haebom Lee, Christian Homeyer, Robert Herzog, Jan Rexilius, and Carsten Rother. Spatio-temporal outdoor lighting aggregation on image sequences using transformer networks. *IJCV*, 131(4):1060–1072, 2023. 4
- [19] Kaican Li, Kai Chen, Haoyu Wang, Lanqing Hong, Chaoqiang Ye, Jianhua Han, Yukuai Chen, Wei Zhang, Chunjing Xu, Dit-Yan Yeung, et al. Coda: A real-world road corner case dataset for object detection in autonomous driving. In *European Conference on Computer Vision*, pages 406–423. Springer, 2022. 1
- [20] Shidi Li, Miaomiao Liu, and Christian Walder. EditVAE: Unsupervised parts-aware controllable 3D point cloud shape generation. In *AAAI*, 2022. 2
- [21] Mingyu Liu, Ekim Yurtsever, Jonathan Fossaert, Xingcheng Zhou, Walter Zimmer, Yuning Cui, Bare Luka Zagar, and Alois C Knoll. A survey on autonomous driving datasets: Statistics, annotation quality, and a future outlook. *IEEE Transactions on Intelligent Vehicles*, 2024. 1
- [22] Thibaut Loiseau, Tuan-Hung Vu, Mickael Chen, Patrick Pérez, and Matthieu Cord. Reliability in semantic segmentation: Can we use synthetic data? In *European Conference on Computer Vision*, pages 442–459. Springer, 2024. 1
- [23] David Lopez-Paz and Maxime Oquab. Revisiting classifier two-sample tests. In *ICLR*, 2018. 5, 16
- [24] Calvin Luo. Understanding diffusion models: A unified perspective. *arXiv preprint arXiv:2208.11970*, 2022. 12, 13
- [25] Shitong Luo and Wei Hu. Diffusion probabilistic models for 3D point cloud generation. In *CVPR*, 2021. 2, 4

- [26] Sivabalan Manivasagam, Shenlong Wang, Kelvin Wong, Wenyan Zeng, Mikita Sazanovich, Shuhan Tan, Bin Yang, Wei-Chiu Ma, and Raquel Urtasun. LiDARsim: Realistic lidar simulation by leveraging the real world. In *CVPR*, 2020. 1, 2, 3
- [27] Shentong Mo, Enze Xie, Ruihang Chu, Lanqing Hong, Matthias Niessner, and Zhenguo Li. DIT-3D: Exploring plain diffusion transformers for 3D shape generation. In *NeurIPS*, 2023. 2, 3, 4, 7, 14, 17
- [28] Khan Muhammad, Tanveer Hussain, Hayat Ullah, Javier Del Ser, Mahdi Rezaei, Neeraj Kumar, Mohammad Hijji, Paolo Bellavista, and Victor Hugo C de Albuquerque. Vision-based semantic segmentation in scene understanding for autonomous driving: Recent achievements, challenges, and outlooks. *IEEE Transactions on Intelligent Transportation Systems*, 23(12):22694–22715, 2022. 1
- [29] Kazuto Nakashima and Ryo Kurazume. Lidar data synthesis with denoising diffusion probabilistic models. In *ICML*, 2024. 2
- [30] Michael Niemeyer and Andreas Geiger. Giraffe: Representing scenes as compositional generative neural feature fields. In *Proceedings of the IEEE/CVF conference on computer vision and pattern recognition*, pages 11453–11464, 2021. 1
- [31] Lucas Nunes, Rodrigo Marcuzzi, Benedikt Mersch, Jens Behley, and Cyrill Stachniss. Scaling diffusion models to real-world 3D lidar scene completion. In *CVPR*, 2024. 2, 4, 7, 12, 14
- [32] William Peebles and Saining Xie. Scalable diffusion models with transformers. In *ICCV*, 2023. 1, 4, 12, 13, 15
- [33] Charles R Qi, Hao Su, Kaichun Mo, and Leonidas J Guibas. PointNet: Deep learning on point sets for 3D classification and segmentation. In *CVPR*, 2017. 4, 5, 16
- [34] Haoxi Ran, Vitor Guizilini, and Yue Wang. Towards realistic scene generation with lidar diffusion models. In *CVPR*, 2024. 2
- [35] Jeremy Reizenstein, Roman Shapovalov, Philipp Henzler, Luca Sbordone, Patrick Labatut, and David Novotny. Common objects in 3d: Large-scale learning and evaluation of real-life 3d category reconstruction. In *Proceedings of the IEEE/CVF international conference on computer vision*, pages 10901–10911, 2021. 2
- [36] Nermin Samet, Oriane Siméoni, Gilles Puy, Georgy Pomiatkin, Renaud Marlet, and Vincent Lepetit. You never get a second chance to make a good first impression: Seeding active learning for 3D semantic segmentation. In *ICCV*, 2023. 7
- [37] Dong Wook Shu, Sung Woo Park, and Junseok Kwon. 3D point cloud generative adversarial network based on tree structured graph convolutions. In *ICCV*, 2019. 2, 5, 16
- [38] Jascha Sohl-Dickstein, Eric Weiss, Niru Maheswaranathan, and Surya Ganguli. Deep unsupervised learning using nonequilibrium thermodynamics. In *International conference on machine learning*, pages 2256–2265. PMLR, 2015. 12
- [39] Yang Song, Jascha Sohl-Dickstein, Diederik P Kingma, Abhishek Kumar, Stefano Ermon, and Ben Poole. Score-based generative modeling through stochastic differential equations. *arXiv preprint arXiv:2011.13456*, 2020. 12, 13
- [40] Matthew Tancik, Pratul P. Srinivasan, Ben Mildenhall, Sara Fridovich-Keil, Nithin Raghavan, Utkarsh Singhal, Ravi Ramamoorthi, Jonathan T. Barron, and Ren Ng. Fourier features let networks learn high frequency functions in low dimensional domains. In *NeurIPS*, 2020. 4
- [41] Haotian Tang, Zhijian Liu, Shengyu Zhao, Yujun Lin, Ji Lin, Hanrui Wang, and Song Han. Searching efficient 3d architectures with sparse point-voxel convolution. In *ECCV*, 2020. 7
- [42] Michał J Tyszkiewicz, Pascal Fua, and Eduard Trulls. GECCO: Geometrically-conditioned point diffusion models. In *ICCV*, 2023. 2
- [43] Ozan Unal, Dengxin Dai, Ali Tamer Unal, and Luc Van Gool. Discwise active learning for lidar semantic segmentation. *IEEE Robotics and Automation Letters (RA-L)*, 8(11):7671–7678, 2023. 7
- [44] Arash Vahdat, Francis Williams, Zan Gojcic, Or Litany, Sanja Fidler, Karsten Kreis, et al. LION: Latent point diffusion models for 3D shape generation. In *NeurIPS*, 2022. 2, 15
- [45] Ashish Vaswani. Attention is all you need. *arXiv preprint arXiv:1706.03762*, 2017. 13
- [46] Kasi Viswanath, Peng Jiang, and Srikanth Saripalli. Reflectivity is all you need!: Advancing lidar semantic segmentation. *arXiv preprint arXiv:2403.13188*, 2024. 2
- [47] Yang Wu, Kaihua Zhang, Jianjun Qian, Jin Xie, and Jian Yang. Text2lidar: Text-guided lidar point cloud generation via equirectangular transformer. In *European Conference on Computer Vision*, pages 291–310. Springer, 2024. 2, 3
- [48] Zhirong Wu, Shuran Song, Aditya Khosla, Fisher Yu, Linguang Zhang, Xiaoou Tang, and Jianxiong Xiao. 3D ShapeNets: A deep representation for volumetric shapes. In *CVPR*, 2015. 2
- [49] Zhengkang Xiang, Zexian Huang, and Kourosh Khoshdelham. Synthetic lidar point cloud generation using deep generative models for improved driving scene object recognition. *Image and Vision Computing*, 150, 2024. 3
- [50] Binhui Xie, Shuang Li, Qingju Guo, Chi Harold Liu, and Xinjing Cheng. Annotator: An generic active learning baseline for lidar semantic segmentation. In *NeurIPS*, 2023. 7
- [51] Yuwen Xiong, Wei-Chiu Ma, Jingkan Wang, and Raquel Urtasun. UltraLiDAR: Learning compact representations for lidar completion and generation. In *CVPR*, 2023. 2, 3

- [52] Guandao Yang, Xun Huang, Zekun Hao, Ming-Yu Liu, Serge Belongie, and Bharath Hariharan. PointFlow: 3D point cloud generation with continuous normalizing flows. In *ICCV*, 2019. [2](#), [5](#), [15](#), [16](#)
- [53] Xiangyu Yue, Bichen Wu, Sanjit A. Seshia, Kurt Keutzer, and Alberto L. Sangiovanni-Vincentelli. A lidar point cloud generator: from a virtual world to autonomous driving. In *ACM International Conference on Multimedia Retrieval (ICMR)*, 2018. [2](#)
- [54] Jinlai Zhang, Lyujie Chen, Bo Ouyang, Binbin Liu, Jihong Zhu, Yujin Chen, Yanmei Meng, and Danfeng Wu. PointCutMix: Regularization strategy for point cloud classification. *Neurocomputing*, 505:58–67, 2022. [1](#)
- [55] Junge Zhang, Feihu Zhang, Shaochen Kuang, and Li Zhang. NeRF-LiDAR: Generating realistic lidar point clouds with neural radiance fields. In *AAAI*, 2024. [2](#)
- [56] Linqi Zhou, Yilun Du, and Jiajun Wu. 3D shape generation and completion through point-voxel diffusion. In *ICCV*, 2021. [15](#)
- [57] Vlas Zyrianov, Xiyue Zhu, and Shenlong Wang. Learning to generate realistic lidar point cloud. In *ECCV*, 2022. [2](#)
- [58] Vlas Zyrianov, Henry Che, Zhijian Liu, and Shenlong Wang. LidarDM: Generative lidar simulation in a generated world. *arXiv preprint arXiv:2404.02903*, 2024. [2](#)

This appendix is organized as follows.

- Appendix A provides some background on diffusion and in particular on transformer-based diffusion.
- Appendix B provides more implementation details.
- Appendix C offers definitions and formulas for the metrics we used.
- Appendix D provides various statistics regarding the distribution of objects we evaluate on.
- Appendix E presents an experimental comparison between training single-model-per-class and a multi-class model.
- Appendix F gives classwise results and includes more qualitative examples.

## A. Background on diffusion

Diffusion has become a common approach for generation at large, and this paper relies on standard diffusion techniques to do so, namely DDPM [14], Classifier Free Guidance [13] and DiT [32]. The novelty that we introduce is at the level of LiDAR object parameterization, including point embeddings (Sec. 3.1), and architecture of the diffusion transformer (Sec. 3.3). Nevertheless, to make the paper (with its appendix) more self-contained, we include here a some background on these techniques. We also provide some details on PixArt- $\alpha$  and DiT-3D, from which we draw inspiration and base some of our baselines.

### A.1. Diffusion process

Generative modeling via the diffusion objective, introduced in [38, 39], has been demonstrated to learn high-quality approximations of data-generating distributions, sufficient to claim the state of the art in a variety of generative tasks. The diffusion process was originally formulated as a continuous process modeled on stochastic differential equations. Interest and development in the topic have led to a confluence of different interpretations of the process, including a time discrete process known as Denoising Diffusion Probabilistic Models, or DDPM [14]. Our work focuses on the time-discrete formulation. However, as noted in [17], this choice of formulation is largely orthogonal to other design choices, and the sampler and specific diffusion process propose different possible directions to take the model design. We chose to rely on DDPM as it was previously used in LiDAR scan generation literature [31].

Generally, the diffusion process entails the corruption of data by iteratively adding Gaussian noise, arriving fi-

nally at data distributed according to a standard Gaussian. A model then learns to reverse this destructive process via iterative denoising steps. This allows the generation of novel samples from the data distribution by sampling noise and applying the denoising process.

### A.2. Time-discrete vs time-continuous diffusion

The time-discrete vs time-continuous options imply the background in which the diffusion process is formulated. Under the continuous-time formulation, the forward process is typically a stochastic differential equation that transforms data into noise. The reverse process can then be computed via Langevin Monte Carlo Markov chain sampling in order to arrive at the denoised sample [39]. Under the discrete-time formulation, the forward process is assumed to be a discrete Markov chain. Under this assumption the process can be modeled via a hierarchical variational auto-encoder with specific restrictions on the data. The data dimension and latent dimension are exactly equal, the latent structure is pre-defined as a Gaussian distribution, and the parameters of the Gaussian are controlled such that at the final step  $T$  of the Markov chain, the latent is equivalent to the standard normal distribution  $\mathcal{N}(\mathbf{0}, \mathbf{I})$  [24].

The above assumptions assist in the simplification of the optimization process. Similar to other VAEs, the approximation of the generative distribution  $\log(p(x))$  is optimized via the Evidence Lower Bound (ELBO) [24]. Under the assumptions on the shape and underlying distribution of the discrete Markov chain above, optimizing the ELBO simplifies to minimizing the Kullback Leibler divergence (KL) between the forward destructive process and the backwards generative process. And given that both distributions are assumed to be Gaussian, optimizing the KL becomes a simple mean squared error loss.

### A.3. Denoising neural network

We define the forward destructive process with a distribution  $q(x_t|x_{t-1})$  at step  $t$  for a dataset sample  $x$ . The associated Markov chain  $\{x_0 \dots x_t \dots x_T\}$  is defined such that  $q(x_t|x_{t-1}) = \mathcal{N}(x_t; \sqrt{1 - \beta_t}x_{t-1}, \beta_t \mathbf{I})$  where  $0 < \dots < \beta_t < \dots < \beta_T < 1$  defines a scaling schedule for the applied noise. This forward process can be re-written such that each time step depends only on the original data via the introduction of  $\alpha_i = 1 - \beta_i$  and  $\bar{\alpha}_t = \prod_{i=1}^t \alpha_i$  such that  $q(x_t|x_0) = \mathcal{N}(x_t; \sqrt{\bar{\alpha}_t}x_0, (1 - \bar{\alpha}_t)\mathbf{I})$ . Given Gaussian noise  $\epsilon_0 \sim \mathcal{N}(\mathbf{0}, \mathbf{I})$ , the reparameterization trick can then be recursively applied to derive a closed form of any  $x_t$  as explained in [24]:

$$x_t = \sqrt{\bar{\alpha}_t}x_0 + \sqrt{1 - \bar{\alpha}_t}\epsilon_0. \quad (1)$$



Via the assumptions above on the structure of the Hierarchical VAE, the reverse diffusion process then can be defined by a separate discrete Markov chain as

$$p(x_{t-1}|x_t) = \mathcal{N}(x_{t-1}; \mu_q(x_t, x_0), \Sigma_q(t)) \quad (2)$$

where  $\mu_q$  is a function of both  $x_t$  and  $x_0$ , and  $\Sigma_q(t) = \sigma_q^2(t)\mathbf{I}$  where

$$\sigma_q^2(t) = (1 - \alpha_t)(1 - \bar{\alpha}_{t-1})/(1 - \bar{\alpha}_t). \quad (3)$$

However, in the generative case, we do not have access to the ground truth  $x_0$  and must construct a corresponding  $\mu_\theta(x_t, t)$ , which predicts  $\mu_q(x_t, x_0)$  and depends only on  $x_t$ , via the application of Eq. (1). This  $\mu_\theta$  is learned via a Denoising Neural Network.

Computing this  $\mu_\theta(x_t, t)$  requires learning an estimation  $\hat{x}_\theta(x_t, t)$  of the original  $x_0$ . This can be further simplified via an additional application of the reparameterization trick such that, instead of learning  $\hat{x}_\theta(x_t, t)$ , the goal is to learn a function  $\hat{\epsilon}_\theta(x_t, t)$  to predict the source noise  $\epsilon_0$ , i.e., the noise that when added to  $x_0$  produces  $x_t$ . Given all of the simplifications on  $\mu_\theta(x_t, t)$ , the final ELBO objective becomes [24]:

$$\arg \min \|\epsilon_0 - \hat{\epsilon}_\theta(x_t, t)\|_2^2 \quad (4)$$

This estimated noise  $\hat{\epsilon}_\theta(x_t, t)$  enables the computation of the mean

$$\mu_\theta(x_t, t) = \frac{1}{\sqrt{\alpha_t}}x_t - \frac{1 - \alpha_t}{\sqrt{1 - \bar{\alpha}_t}\sqrt{\alpha_t}}\hat{\epsilon}_\theta(x_t, t), \quad (5)$$

which in turn provides the denoising step:

$$x_{t-1} = \frac{1}{\sqrt{\alpha_t}} \left( x_t - \frac{1 - \alpha_t}{\sqrt{1 - \bar{\alpha}_t}} \hat{\epsilon}_\theta(x_t, t) \right) + \sigma_t \epsilon_0. \quad (6)$$

#### A.4. Guiding the diffusion process

Under the continuous-time interpretation, the diffusion process can be described as a direction through the latent space, from a standard Gaussian Distribution towards the data generating distribution [39]. This direction formulation ties directly into the use of conditioning information to guide the diffusion process. The conditioning information changes the direction through the latent spaces towards a specific part of the data generating distribution.

Several methods of guidance have been proposed. This work relies on Classifier Free Guidance [13]. Under the Classifier Free Guidance formulation, two separate diffusion models estimate the noise added to the same example. The first model is unconditioned, and

the second uses the conditioning information. By evaluating the difference between the predicted noise by both models, the direction enforced by the conditioning information is found. A utility parameter  $\lambda \geq 0$  then controls the degree to which the conditioning information is used during inference.

The result is that, during sampling, the estimated noise is predicted using:

$$\hat{\epsilon}_\theta(x_t, t) + \lambda(\hat{\epsilon}_\theta(x_t, t, y) - \hat{\epsilon}_\theta(x_t, t)). \quad (7)$$

Ultimately it is not necessary to train two different diffusion models. During the training procedure, the conditioning information is replaced by a null token in a manner which imitates random dropout. A single diffusion model is thus capable of performing Classifier Free Guidance [24].

#### A.5. Diffusion transformer

**DiT.** In [32], Peebles et al. introduced a scalable denoising architecture based on the transformer [45]. The authors demonstrate that the attention mechanism can be adapted to predict added noise to 2D images, and then trained via the diffusion objective to produce a state of the art 2D image generation model. This work contrasts with previous diffusion methodology by focusing on architectural choices in regards to both the quality of the generated results and the scalability of the model. Prior to the introduction of the Diffusion Transformer (DiT), most works applied the diffusion objective via a denoising U-Net, i.e., a classical convolutional U-Net trained to predict added noise to an image. The novel architecture of the DiT is shown in Fig. 5 (left) of this appendix. DiT uses a standard self-attention layer followed by a feed-forward architecture, but uses adaptive layer-norm layers to propagate conditioning information, such as the time step or class label. The conditioning information is used to the scale and shift parameters of the normalization layers via an MLP. Applying conditioning information in adaptive normalization layers is a trick introduced first by StyleGAN [16], and remains a popular method for applying conditioning information.

**PixArt- $\alpha$ .** A state-of-the-art variant of the Diffusion Transformer, modified to use text prompts as conditioning, was introduced in [5]. This model, called PixArt- $\alpha$ , introduces cross-attention layers between the input features and the embedded text prompts to guide the diffusion process. The authors also introduce an optimization of the adaptive layer norm architecture, where a single MLP is used to learn the scale and shift parameters for the entire model. Fig. 6 of this appendix shows the architecture of this model. PixArt- $\alpha$  is significant to LiDAR

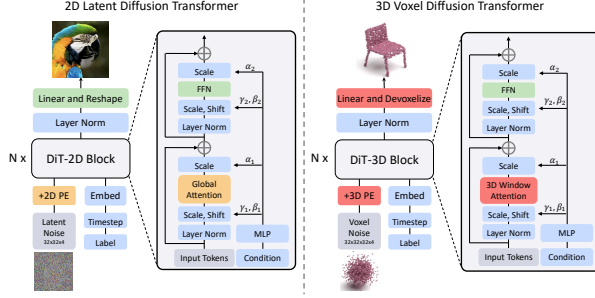


Figure 5. Comparison of two Diffusion Transformer architectures. On the left is the classic 2D DiT. Patch embeddings are fed into classical self-attention layers. Note the Adaptive Layer Norm layers to apply conditioning information. On the right is the DiT-3D, which introduces a voxelization step to embed 3D data. (The image is taken from [27].)

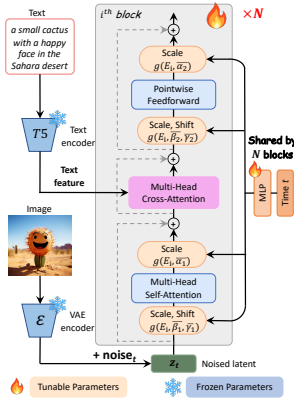


Figure 6. The PixArt- $\alpha$  architecture, from [5]. Note the shared shift and scale parameters and the introduction of cross attention layers to propagate conditioning via text tokens. (The image is taken from [5].)

object generation because it provides guidelines for how to apply more complex conditioning guidance. The original DiT paper uses only class labels as conditioning.

**DiT-3D.** The Diffusion Transformer has been adapted for a 3D shape generation task, where it achieves state-of-the-art results [27]. This DiT-3D introduces a voxelization step, which converts the unstructured 3D point cloud data into features of a  $32 \times 32 \times 32$  voxel grid. These voxels are then grouped into patches and embedded. This makes it possible to use more or less the same overall architecture as the Diffusion Transformer, using the same adaptive Layer Norm layers to apply conditioning information (cf. Fig. 5 (right) of this appendix). This allows the leveraging of models pre-trained on large 2D datasets for 3D generative tasks.

**3D diffusion transformers.** The significant aspects of the Diffusion Transformer architecture, in regards to the LiDAR object generation task, can be summarized as follows:

- *Easily scalable:* DiT-based architectures build upon the wealth of literature regarding the scaling of parameter size of transformer based architectures. This is especially important in LiDAR object generation where the variability in point cloud sizes between objects at different locations makes memory consumption per batch highly irregular. Thus it is useful to be able to train small models with the justified expectation of improved performance with increased size.
- *Positional embeddings by default:* In the LiDAR object generation task, absolute positioning information is inherent to the conditioning of the model. Transformer architectures include explicit layers to encode absolute position information into the training process, and thus this absolute positional knowledge is provided by default to the model.

**Architecture of LOGen, DiT-3DL and PixArt-L** Our baselines DiT-3DL and PixArt-L, whose architecture is shown Fig. 7 together with LOGen, are directly adapted from their original counterparts to handle: (i) LiDAR data, i.e., point embedding, and (ii) LiDAR object conditioning. LOGen is then a modification of PixArt-L, as described in main paper.

## B. Implementation details

**Sparse convolutional architecture.** For experiments using a sparse convolutional architecture, we follow the same model structure and size as LiDiff [31], using MinkUNet, the sparse convolutional U-Net introduced in [6]. The additional conditioning information is concatenated onto the time step information. The MinkUNet models contain roughly 36M parameters.

**Transformer architectures.** Unless otherwise stated, the transformer architectures used were extra small (XS) variants of the DiT. These models contain 12 transformer blocks, each with 3 heads, and an embedding dimension of 192. Where voxelization was used, a patch size of 4 was used. This means that four voxels were combined into a single patch. The XS transformer variants contain roughly 7.5M parameters.

To apply the additional conditioning information when testing vanilla DiT-3D variants, the new conditions were embedded and then concatenated to the time step. The resulting vector was then flattened and used as input to the MLP to learn the adaptive layer-norm parameters. For the cross-attention variants, the condition

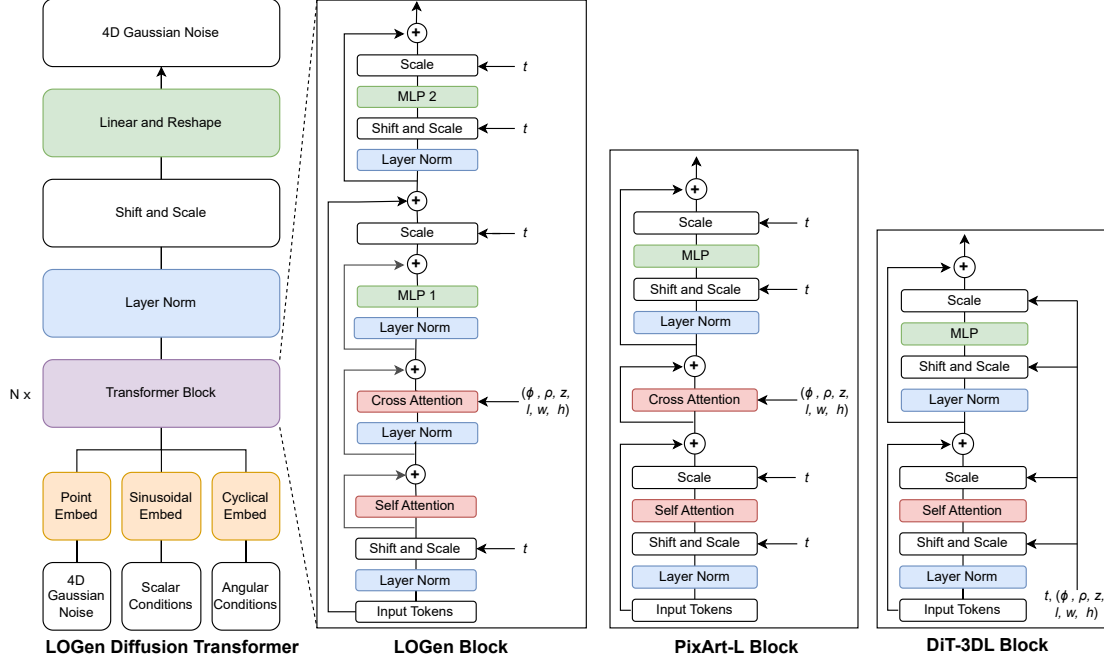


Figure 7. Architecture of LOGen and baselines PixArt-L and DiT-3DL.

was used as input only to the cross-attention layers and the adaptive layer-norm was learned only using the time step. For all variants, the adaptive layer-norm MLP was initialized to zero following [32].

**Diffusion parameters.** The DDPM scheduler was used with 1000 time steps during training. During inference 500 time steps were used. The  $\beta$  schedule was linearly spread on the range of  $[3.5 \cdot 10^{-5}, 0.007]$ , as in LiDiff. The parameter  $\lambda$  controlling the strength of the guidance was set to 1.0 (best value from a grid search, while LiDiff uses  $\lambda = 6.0$ ). This value of  $\lambda$  cancels out the unconditional score term in Eq. (7). However, this equation is only used during the sampling procedure (which we do at inference or validation). During training, we periodically use null conditions for 10% of the conditions in a batch (as LiDiff does). So the classifier free guidance does have an impact on the training procedure.

**Training.** The Adam optimizer was used with a constant learning rate of 0.0001. We trained small classes (i.e., barrier, bike, car, motorcycle, pedestrian, traffic cone) for 500,000 iterations with a batch size of 16. The remaining large object classes (i.e., bus, construction vehicle, trailer and truck) are trained for 5,000,000 iterations with a batch size 4. All trainings were conducted on 4 Nvidia A100 GPUs.

## C. Metrics

We provide below a formal definition of the metrics used in the paper.

- **Chamfer distance (CD)** and **Earth mover distance (EMD)**:

We evaluate object-level metrics using standard CD and EMD distances to measure the similarity between two point clouds.

$$\text{CD}(X, Y) = \sum_{x \in X} \min_{y \in Y} \|x - y\|_2^2 + \sum_{y \in Y} \min_{x \in X} \|x - y\|_2^2, \quad (8)$$

$$\text{EMD}(X, Y) = \min_{\gamma: X \rightarrow Y} \sum_{x \in X} \|x - \gamma(x)\|_2, \quad (9)$$

where  $\gamma$  is a bijection between point clouds  $X$  and  $Y$ . (To follow previous work in this domain [44, 52, 56], we use the square distance for the CD computation.)

- **Coverage (COV)**:

Given a set of real object samples  $S_r$  and a set of generated objects  $S_g$ , COV [1] measures the proportion of real pointsets in  $S_r$  matched to at least one generated pointset in  $S_g$ . Although COV does not assess the

quality of the generated pointsets, it serves as a metric to quantify its diversity. Some low-quality sets of point clouds can however obtain high COV scores.

$$\text{COV}(S_g, S_r) = \frac{|\{\arg \min_{Y \in S_r} D(X, Y) | X \in S_g\}|}{|S_r|}. \quad (10)$$

In our experiments, we have used both CD and EMD to compute  $D(\cdot, \cdot)$ . For  $S_r$ , we use all objects of a given class, and for  $S_g$ , we generate as one sample per sample in  $S_r$  with corresponding conditioning.

- **1-nearest neighbor accuracy (1-NNA):**

1-NNA [23, 52] evaluates both the diversity and quality aspects in a single metric. Like COV, it relies on two sets  $S_r$  and  $S_g$  of, respectively, real and generated pointsets. Real and synthetic objects are merged and 1-NNA calculates the proportion of nearest neighbors for each sample that come from the same source. The 1-NNA score ranges from 100%, when the distributions are distinct, to 50%, when they are indistinguishable.

$$\text{1-NNA}(S_g, S_r) = \frac{\sum_{X \in S_g} \mathbb{I}[N_X \in S_g] + \sum_{Y \in S_r} \mathbb{I}[N_Y \in S_r]}{|S_g| + |S_r|}, \quad (11)$$

where  $\mathbb{I}[\cdot]$  denotes the indicator function and  $N_X$  represents the nearest neighbor of point cloud  $X$  in the set  $(S_r \cup S_g) \setminus \{X\}$ . In our experiments, we have used both CD and EMD as distance metrics to calculate the nearest neighbors, and  $S_r$  and  $S_g$  are defined as for COV.

- **Fréchet Point Cloud Distance (FPD)**

FPD [37] is an adaptation of the classic Fréchet Inception Distance (FID) [12], where 2D Inception features are replaced with 3D PointNet features [33]. Like FID, FPD computes the 2-Wasserstein distance between the real and generated Gaussian distributions in the feature space.

$$\text{FPD}(S_r, S_g) = \|\mathbf{m}_{S_r} - \mathbf{m}_{S_g}\|_2^2 + \text{Tr}(\Sigma_{S_r} + \Sigma_{S_g} - 2(\Sigma_{S_r} \Sigma_{S_g})^{\frac{1}{2}}), \quad (12)$$

where  $\mathbf{m}_{S_r}$  and  $\Sigma_{S_r}$  represent the mean vector and covariance matrix of the points calculated from real point clouds in  $S_r$ , while  $\mathbf{m}_{S_g}$  and  $\Sigma_{S_g}$  are the mean vector and covariance matrix calculated from generated point clouds in  $S_g$ .  $\text{Tr}(A)$  is the sum of the elements along the main diagonal of matrix  $A$ .

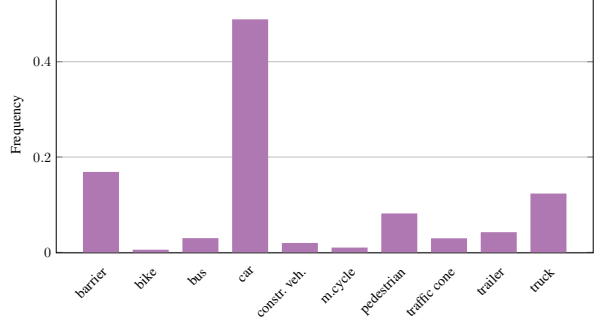


Figure 8. **Frequency of objects per class** in nuScenes, considering objects with at least 20 points.

The original FPD is based on the PointNet classifier trained on ModelNet-40 [33] with dense and uniform point sampling. To account for the sparse and non-uniform characteristics of LiDAR-scanned objects in nuScenes, we instead use a separate PointNet classifier that has been trained on the real LiDAR data from nuScenes. Like with the original FPD, we extract a 1803-dimensional feature vector (5 fewer dimensions than the original 1808, due to the presence of 5 fewer classes) from the output of the dense layers, to calculate the mean and covariance in Eq. (12).

- **Kernel Point Cloud Distance (KPD)**

We define KPD by adapting the Kernel Inception Distance (KID) [2], where 2D Inception features are replaced with our 1803-dimensional 3D PointNet features. Like KID, KPD calculates the maximum mean discrepancy (MMD) between the real and generated instances in the feature space.

$$\text{KID}(S_r, S_g) = \text{MMD}(S_r, S_g)^2. \quad (13)$$

## D. Distribution of evaluated objects

In LiDAR datasets, the number of objects displays large variations among classes, not to mention the number of points in these objects depending on the classes, distance to the sensor and orientation. As an illustration, the classwise frequency of objects in nuScenes is pictured on Fig. 8 of this appendix. More statistics are available in [3].

In nuScenes data, some objects can have as few as 1 point. Although some of our experiments (not reported here) went as low as keeping objects with at least 5 points, evaluating the quality of generation with so few points makes little sense. Therefore, we set a minimum



threshold to 20 points for an object to be used for training and for evaluation, which covers more than 95% of all object points. It can also be noted that the official instance segmentation evaluation of nuScenes only considers instances with at least 15 points [10].

Full statistics regarding the number of points and objects are available in Tab. 7 of this appendix.

## E. One multi-class vs Single model per class

Training single model per class allows us to focus on specific classes, maintain consistent batch sizes with minimal zero-padding, keep the network compact (7.5M parameters), and reduce overall computational overhead (measured in iterations per instance). However, a multi-class model of the same size and trained with the same number of iterations does not perform as well as a single model per class, as shown in Table 6. Notably, training single model per class introduces no drawbacks in terms of runtime or model efficiency. We note that DiT3D [27] similarly provides mostly class-wise results.

## F. Detailed results

### F.1. Classwise numbers

We provide complementary class-wise results for all our experiments in the main paper. For additional results on point-based metrics, refer to Table 8, Table 9, Table 10, and Table 11. For feature-based metrics, see Table 12, Table 13, and Table 14. Finally, for complementary results on the evaluation of conditioning on distance to sensor refer to Table 15, Table 16, Table 17, and evaluation of conditioning on sensor viewing angle is presented in Table 18.

### F.2. More qualitative examples

In Figure 9, we present novel objects produced by LO-Gen for the remaining classes. To get a better sense of our 3D generations, please refer to the accompanying video results.

LOGen PE <sub>4ch</sub>	CD ↓ EMD ↓	1-NNA ↓ CD	COV ↑ EMD	FPD ↓ 3 ch.	KPD ↓ 4 ch.	APC ↑ 3 ch.
Single-model-per-class	<b>0.130 0.111</b>	74.1	70.6	36.0	42.3	<b>1.34 2.18 0.10 0.12</b>
Multi-class model	0.149 0.134	<b>72.8</b>	<b>68.9</b>	<b>37.1</b>	<b>43.3</b>	2.35 4.28 0.21 0.45 36.2 42.5

Table 6. **Single-model-per-class vs. multi-class model.** Comparison of a same size single-model-per-class and multi-class models on generation metrics. The multi-class model lags behind the single-model-per-class approach in realism metrics.

	obj. size  s  < 20 pts		objects size  s  ≥ 20 points					
Class	total no. pts	total no. obj.	min no. pts	median no. pts	mean no. pts	max no. pts	total no. pts	total no. obj.
barrier	493,786	78,087	20	62	163	2,667	7,422,517	45,350
bicycle	41,078	8,021	20	36	57	838	86,997	1,506
bus	46,248	6,381	20	96	536	11,587	4,309,567	8,030
car	1,263,050	231,531	20	81	264	8,695	34,783,810	131,366
constr. vehicle	46,194	6,932	20	69	209	8,641	1,108,460	5,300
motorcycle	42,679	7,620	20	59	135	1,952	368,415	2,709
pedestrian	753,031	165,449	20	37	64	1,192	1,408,328	21,942
traffic cone	229,178	62,951	20	39	51	726	408,092	7,931
trailer	66,359	9,310	20	85	380	10,825	4,333,342	11,378
truck	251,543	39,061	20	81	428	10,719	14,197,897	33,172
Overall	3,233,146	615,343	20	65	254	11,587	68,427,425	268,684

Table 7. **Distribution of object data in nuScenes.** We provide detailed statistics on objects with at least 20 points, which we use for our generation (training and testing). Objects with at least 20 points represent 95.5% of all object points.

	Model	Emb.	bar.	bic.	bus	car	c.veh	mot.	ped.	t.con.	tra.	tru.	mean
CD	MinkUNet		0.16	0.22	0.19	0.14	0.2	0.19	0.26	0.32	0.23	0.17	0.208
	DiT-3DL	VE <sub>3ch</sub>	0.09	0.13	0.19	0.17	0.11	0.11	0.11	0.09	0.2	0.15	0.136
	DiT-3DL	PE <sub>4ch</sub>	0.08	0.13	0.19	0.13	0.17	0.11	0.13	0.1	0.21	0.17	0.142
	PixArt-L	PE <sub>4ch</sub>	0.12	0.16	0.31	0.25	0.21	0.15	0.13	0.13	0.26	0.24	0.196
	LOGen	PE <sub>4ch</sub>	0.08	0.12	0.15	0.13	0.15	0.11	0.11	0.09	0.2	0.16	0.130
EMD	MinkUNet		0.16	0.22	0.2	0.13	0.2	0.19	0.27	0.35	0.24	0.16	0.212
	DiT-3DL	VE <sub>3ch</sub>	0.07	0.1	0.2	0.11	0.16	0.08	0.08	0.06	0.2	0.15	0.121
	DiT-3DL	PE <sub>4ch</sub>	0.06	0.09	0.21	0.11	0.15	0.08	0.1	0.07	0.21	0.17	0.125
	PixArt-L	PE <sub>4ch</sub>	0.1	0.13	0.39	0.3	0.22	0.14	0.1	0.1	0.29	0.27	0.204
	LOGen	PE <sub>4ch</sub>	0.06	0.08	0.15	0.11	0.14	0.08	0.08	0.06	0.19	0.16	0.111

Table 8. **Point-based metrics.** [Complement to Table 1 in the paper] We present class-wise results of CD and EMD.

	Model	Emb.	bar.	bic.	bus	car	c.veh	mot.	ped.	t.con.	tra.	tru.	mean
CD	MinkUNet		77.1	75.8	83.7	72.3	81.7	82.7	79.3	80.2	84.6	77.4	79.5
	DiT-3DL	VE <sub>3ch</sub>	73.2	71.1	79.2	77.4	85.4	71.6	70.8	65.3	83.1	80.2	75.8
	DiT-3DL	PE <sub>4ch</sub>	68.6	72.8	76.5	71.2	82.2	71.6	69.4	64.8	80.0	76.8	73.4
	PixArt-L	PE <sub>4ch</sub>	75.5	78.0	76.8	72.6	84.7	73.2	73.1	71.9	82.6	76.4	76.5
	LOGen	PE <sub>4ch</sub>	67.4	75.8	76.1	71.6	87.7	73.3	66.3	64.9	83.2	73.7	74.1
EMD	MinkUNet		71.0	70.5	81.7	67.4	74.3	74.7	74.0	77.8	78.0	74.2	74.4
	DiT-3DL	VE <sub>3ch</sub>	64.8	67.7	79.6	73.0	75.4	72.6	62.7	59.6	77.3	75.6	70.9
	DiT-3DL	PE <sub>4ch</sub>	62.4	70.8	79.6	67.8	73.8	73.7	66.8	63.9	74.8	72.7	70.7
	PixArt-L	PE <sub>4ch</sub>	68.6	72.4	82.2	73.8	76.1	69.3	61.0	67.2	79.0	74.8	72.5
	LOGen	PE <sub>4ch</sub>	64.0	69.8	74.3	68.4	82.9	74.7	61.1	59.7	81.0	69.6	70.6

Table 9. **Point-based metrics.** [Complement to Table 1 in the paper] We present class-wise results of 1-NNA.

	Model	Emb.	bar.	bic.	bus	car	c.veh	mot.	ped.	t.con.	tra.	tru.	mean
CD	MinkUNet		34.8	38.2	33.6	38.8	33.7	31.5	25.5	30.7	36.2	33.4	33.7
	DiT-3DL	VE <sub>3ch</sub>	34.7	40.0	27.3	33.4	32.1	39.9	32.5	43.7	30.0	29.0	34.3
	DiT-3DL	PE <sub>4ch</sub>	35.6	38.5	29.2	36.8	32.1	39.5	37.0	42.6	32.5	30.9	35.5
	PixArt-L	PE <sub>4ch</sub>	33.2	40.4	21.3	31.7	31.5	37.3	33.8	41.6	33.0	30.9	33.5
	LOGen	PE <sub>4ch</sub>	38.5	38.5	38.0	37.9	30.4	36.4	35.9	41.0	27.4	35.0	36.0
EMD	MinkUNet		44.4	41.1	44.1	47.2	45.3	42.1	34.5	33.8	40.0	44.3	41.7
	DiT-3DL	VE <sub>3ch</sub>	44.7	44.5	33.9	44.5	42.2	49.0	42.7	42.3	35.6	40.2	42.0
	DiT-3DL	PE <sub>4ch</sub>	45.2	40.0	33.0	43.9	41.7	46.5	47.8	44.4	39.1	38.3	42.1
	PixArt-L	PE <sub>4ch</sub>	44.9	44.5	28.1	40.4	41.9	49.2	46.2	44.1	36.3	42.0	41.8
	LOGen	PE <sub>4ch</sub>	44.45	42.3	40.4	44.2	42.1	46.7	46.0	41.3	32.8	41.7	42.3

Table 10. **Point-based metrics.** [Complement to Table 1 in the paper] We present class-wise results of COV.

	Model	Emb.	bar.	bic.	bus	car	c.veh	mot.	ped.	t.con.	tra.	tru.	mean
1-NNA	DiT-3DL	PE <sub>4ch</sub>	75.0	61.9	76.0	69.7	71.7	68.3	82.6	88.3	77.2	73.1	74.4
	PixArt-L	PE <sub>4ch</sub>	73.9	56.9	80.4	72.0	73.2	66.6	74.9	62.7	76.2	79.2	71.6
	LOGen	PE <sub>4ch</sub>	70.8	60.4	69.0	68.7	70.1	64.79	75.0	62.4	71.7	69.5	68.2
COV	DiT-3DL	PE <sub>4ch</sub>	36.1	38.9	28.8	38.8	35.0	37.9	23.8	15.8	26.7	32.4	31.4
	PixArt-L	PE <sub>4ch</sub>	35.	38.5	27.7	36.6	32.4	37.5	31.2	35.5	28.3	26.6	32.9
	LOGen	PE <sub>4ch</sub>	39.5	39.7	37.4	39.2	40.7	35.7	32.6	32.7	35.5	37.1	37.0

Table 11. **Point-based metrics.** [Complement to Table 1] We present class-wise results of COV and 1-NNA on intensity realism.

	Model	Emb.	bar.	bic.	bus	car	c.veh	mot.	ped.	t.con.	tra.	tru.	mean
3 ch.	MinkUNet		23.15	7.63	8.14	0.32	1.68	8.62	72.06	115.69	13.44	3.23	25.4
	DiT-3DL	VE <sub>3ch</sub>	3.31	2.86	6.08	0.70	2.96	0.87	0.65	0.69	5.78	4.09	2.80
	DiT-3DL	PE <sub>4ch</sub>	3.27	3.19	4.26	0.41	1.32	0.85	3.17	1.76	4.95	2.96	2.62
	PixArt-L	PE <sub>4ch</sub>	0.30	4.11	5.80	1.17	2.42	0.93	1.45	1.13	7.77	4.37	2.95
	LOGen	PE <sub>4ch</sub>	0.37	1.78	1.44	0.60	1.49	0.79	0.14	1.52	4.16	1.02	1.34
4 ch.	DiT-3DL	PE <sub>4ch</sub>	4.73	7.36	4.78	1.52	4.0	4.74	20.09	8.44	9.04	5.16	6.99
	PixArt-L	PE <sub>4ch</sub>	2.67	4.62	10.26	2.19	3.52	2.97	3.18	1.03	11.64	9.46	5.16
	LOGen	PE <sub>4ch</sub>	0.64	3.78	1.89	0.56	3.04	3.03	0.52	0.99	4.93	2.31	2.18

Table 12. **Feature-based metrics.** [Complement to Table 2 in the paper] We present class-wise results of FPD.

	Model	Emb.	bar.	bic.	bus	car	c.veh	mot.	ped.	t.con.	tra.	tru.	mean
3 ch.	MinkUNet		3.68	0.73	0.98	0.00	0.04	1.16	8.34	14.84	1.65	0.43	3.18
	DiT-3DL	VE <sub>3ch</sub>	0.30	0.12	0.61	0.07	0.18	0.02	0.08	0.09	0.54	0.44	0.25
	DiT-3DL	PE <sub>4ch</sub>	0.40	0.17	0.37	0.05	0.04	-0.01	0.49	0.19	0.49	0.28	0.25
	PixArt-L	PE <sub>4ch</sub>	0.01	0.22	0.53	0.12	0.11	0.00	0.16	0.11	0.70	0.48	0.24
	LOGen	PE <sub>4ch</sub>	0.00	0.01	0.23	0.04	0.00	-0.00	-0.01	0.22	0.31	0.22	0.10
4 ch.	DiT-3DL	PE <sub>4ch</sub>	0.49	0.33	0.42	0.10	0.24	0.14	2.80	1.50	0.93	0.53	0.75
	PixArt-L	PE <sub>4ch</sub>	0.18	0.05	0.81	0.15	0.07	0.02	0.39	0.07	1.28	1.04	0.41
	LOGen	PE <sub>4ch</sub>	0.03	0.14	0.11	0.04	0.09	0.02	0.06	0.04	0.48	0.17	0.12

Table 13. **Feature-based metrics.** [Complement to Table 2 in the paper] We present class-wise results of KPD.

	Model	Emb.	bar.	bic.	bus	car	c.veh	mot.	ped.	t.con.	tra.	tru.	mean
3 ch.	MinkUNet		34.4	2.2	3.1	45.1	24.0	10.8	44.9	34.4	14.0	12.9	22.6
	DiT-3DL	VE <sub>3ch</sub>	62.8	5.2	3.6	46.5	34.7	19.8	89.5	93.3	26.1	16.2	39.8
	DiT-3DL	PE <sub>4ch</sub>	63.4	7.1	4.7	42.9	26.1	19.8	86.5	83.8	23.0	14.2	37.2
	PixArt-L	PE <sub>4ch</sub>	65.4	6.7	3.7	39.1	28.9	22.7	81.9	88.3	27.0	14.3	37.8
	LOGen	PE <sub>4ch</sub>	65.7	6.3	7.8	49.4	30.8	19.8	86.3	94.1	32.0	16.1	40.9
	Real dataset objects		66.3	5.6	8.0	45.6	27.5	17.8	83.7	88.5	30.3	16.6	39.0
4 ch.	DiT-3DL	PE <sub>4ch</sub>	71.1	8.6	8.9	45.5	33.6	20.5	80.8	93.9	39.6	13.7	41.7
	PixArt-L	PE <sub>4ch</sub>	71.8	8.9	6.5	46.2	44.4	24.9	93.7	91.5	50.1	15.9	45.5
	LOGen	PE <sub>4ch</sub>	72.9	8.6	9.6	58.5	49.0	24.5	97.7	94.3	49.9	16.4	48.1
	Real dataset objects		73.3	8.23	10.	55.5	42.2	22.0	97.3	91.7	46.5	16.4	46.4

Table 14. **Feature-based metrics.** [Complement to Table 2 in the paper] We present class-wise results of APC.

	Distance to sensor	bar.	bic.	bus	car	c.veh	mot.	ped.	t.con.	tra.	tru.	mean
3 ch.	$d$	0.37	1.78	1.44	0.60	1.49	0.79	0.14	1.52	4.16	1.02	1.34
	$d / 2$	0.44	4.95	2.75	2.72	3.22	1.72	1.13	4.16	5.80	3.94	3.08
	$d \times 1.5$	1.19	1.13	1.46	0.85	2.19	1.45	3.64	0.77	6.19	1.23	2.01
	$d \times 2$	2.80	4.12	2.98	1.80	3.63	3.03	13.53	5.15	8.71	3.63	4.79
4 ch.	$d$	0.64	3.78	1.89	0.56	3.04	3.03	0.52	0.99	4.93	2.31	2.18
	$d / 2$	2.17	9.92	11.88	5.40	9.80	7.01	4.27	4.73	16.68	9.44	8.13
	$d \times 1.5$	1.57	4.48	6.20	4.64	7.35	6.70	8.08	5.65	5.48	6.04	5.62
	$d \times 2$	3.38	11.67	12.23	12.82	13.03	10.64	22.78	17.89	10.28	12.29	12.7

Table 15. **Evaluation of conditioning on distance to sensor.** [Complement to Table 3 in the paper] We present class-wise results of FPD.



Distance to sensor		bar.	bic.	bus	car	c.veh	mot.	ped.	t.con.	tra.	tru.	mean
3 ch.	$d$	0.00	0.01	0.23	0.04	0.00	-0.00	-0.01	0.22	0.31	0.22	0.10
	$d / 2$	0.08	0.54	0.13	0.32	0.20	0.14	0.23	0.81	0.48	0.39	0.33
	$d \times 1.5$	0.13	0.05	0.06	0.02	0.10	0.05	0.67	0.04	0.58	0.06	0.18
	$d \times 2$	0.43	0.41	0.16	0.14	0.34	0.00	2.31	0.98	1.01	0.10	0.61
4 ch.	$d$	0.03	0.14	0.11	0.04	0.09	0.02	0.06	0.04	0.48	0.17	0.12
	$d / 2$	0.08	1.00	1.09	0.74	0.88	0.36	0.73	0.57	2.17	0.91	0.85
	$d \times 1.5$	0.10	0.57	0.63	0.59	0.65	0.59	1.33	0.83	0.37	0.74	0.64
	$d \times 2$	0.42	1.44	1.31	1.92	1.48	1.25	3.66	3.10	0.83	1.69	1.71

Table 16. **Evaluation of conditioning on distance to sensor.** [Complement to Table 3 in the paper] We present class-wise results of KPD.

Distance to sensor		bar.	bic.	bus	car	c.veh	mot.	ped.	t.con.	tra.	tru.	mean
3 ch.	$d$	65.7	6.3	7.8	49.4	30.8	19.8	86.3	94.1	32.0	16.1	40.9
	$d / 2$	67.1	4.9	11.7	46.3	40.1	22.7	90.1	84.5	27.7	17.0	38.3
	$d \times 1.5$	63.6	5.4	5.4	51.1	22.7	18.9	75.5	87.9	33.2	14.5	37.8
	$d \times 2$	60.9	3.2	3.6	53.2	14.3	19.1	66.9	73.7	32.1	12.5	34.0
4 ch.	$d$	72.9	8.6	9.6	58.5	49.0	24.5	97.7	94.3	49.9	16.4	48.1
	$d / 2$	72.8	8.3	17.0	63.0	49.5	23.0	97.7	91.3	56.0	19.4	49.8
	$d \times 1.5$	72.2	8.3	5.1	44.8	39.9	21.8	90.1	82.3	49.0	14.5	42.8
	$d \times 2$	71.1	6.0	4.1	35.1	32.0	22.7	81.2	68.7	49.1	13.8	38.4

Table 17. **Evaluation of conditioning on distance to sensor.** [Complement to Table 3 in the paper] We present class-wise results of APC.

Test Objects Box Orientation			bar.	bic.	bus	car	c.veh	mot.	ped.	t.con.	tra.	tru.	mean
3 channel	real	orig.	80.3	48.8	90.7	94.2	40.6	86.0	085.5	73.4	60.7	85.2	74.5
	LOGen	orig.	78.2	50.9	60.1	79.1	28.1	82.2	84.2	73.5	37.5	63.2	63.7
	LOGen	rot. $1/5$	71.1	45.0	41.1	68.5	19.9	72.6	80.4	67.2	22.7	48.6	53.7
	LOGen	rot. $2/5$	70.1	45.3	40.9	73.7	18.3	73.4	82.0	66.9	27.1	50.5	54.8
	LOGen	rot. $3/5$	71.2	42.4	39.7	65.3	16.5	73.9	81.7	68.8	26.6	52.2	53.8
	LOGen	rot. $4/5$	71.1	41.9	43.7	65.2	19.8	73.6	81.4	67.9	20.9	47.1	53.3
	real	orig.	81.6	50.4	90.9	94.6	44.5	88.1	85.6	77.4	64.6	85.6	76.3
4 channel	LOGen	orig.	78.0	48.9	71.7	91.3	37.1	82.0	84.8	79.1	45.1	72.9	69.1
	LOGen	rot. $1/5$	71.8	46.6	64.0	87.2	32.8	76.5	84.0	75.5	42.7	64.6	64.6
	LOGen	rot. $2/5$	72.5	46.1	64.3	89.2	36.1	81.3	84.2	75.6	41.6	69.5	66.0
	LOGen	rot. $3/5$	73.8	46.9	58.3	87.9	28.6	75.5	84.3	76.1	43.4	63.3	63.8
	LOGen	rot. $4/5$	72.0	44.5	66.7	84.9	32.6	78.9	83.8	74.5	39.8	63.3	64.1

Table 18. **Evaluation of conditioning on sensor viewing angle.** [Complement to Table 5 in the paper] We present per class mIoU performances.

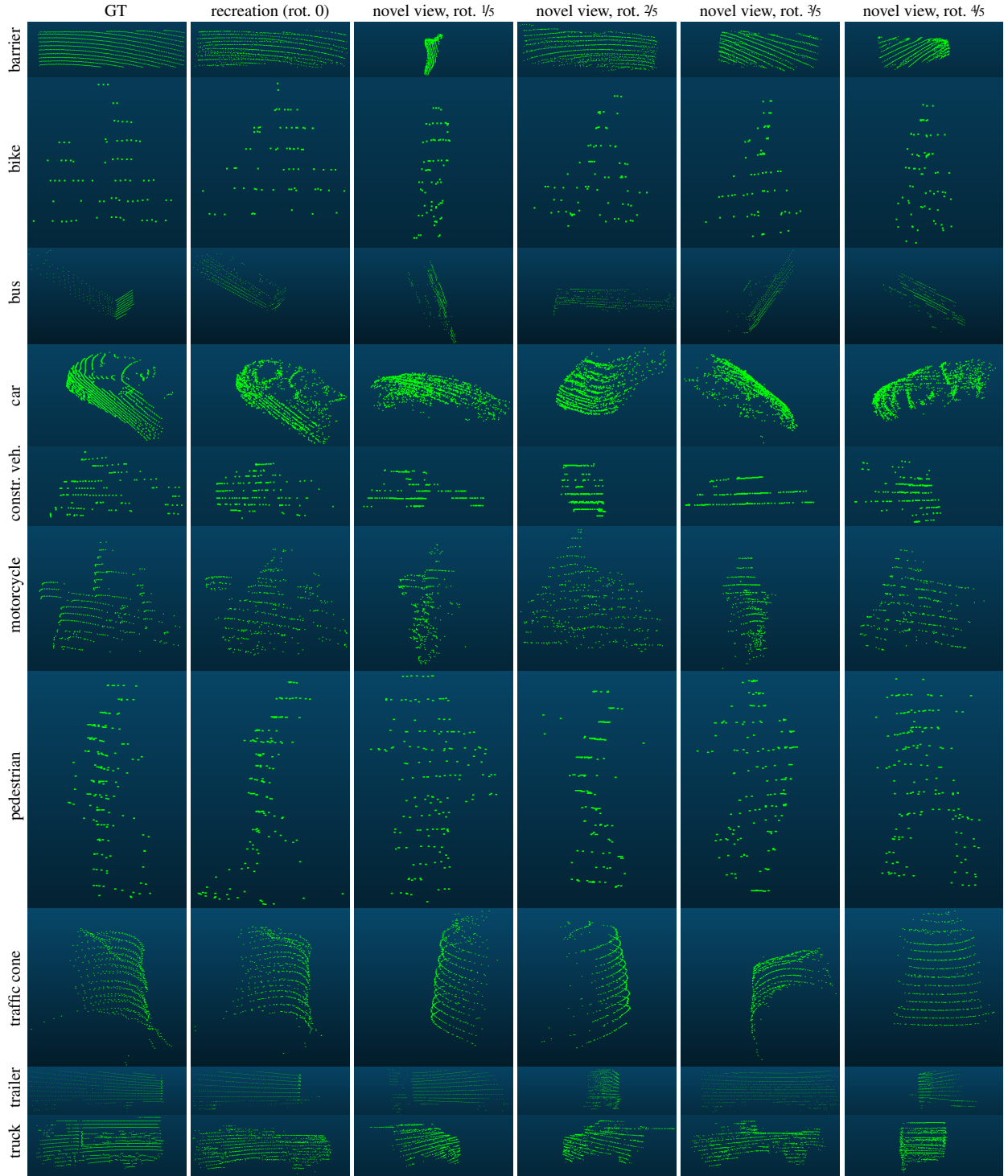


Figure 9. **Novel objects produced by LOGen.** Recreations are generated using the conditioning information  $\kappa$  of a real object, the rest of the objects are created from novel views by interpolating the viewing angle  $\phi$  of the condition.